

Chapter 2

Phase-contrast imaging

2.1 Introduction

A quick look through the JILA theses on atom trapping and cooling shows that every one covers the topic of optical imaging in one way or another; this thesis is no exception. The reason is obvious: essentially all experimental data on an atom cloud derives from images formed by scattering probe laser light off it. Every new imaging technique opens up new experimental possibilities. Phase-contrast imaging [2], allowing the non-destructive measurement of condensate samples *in situ* [52], has proven to be a particularly useful and general technique for our experimental apparatus, especially for the vortex experiments detailed in this thesis. Because phase-contrast imaging has become the workhorse for condensate assay in our experiment, more than the usual detail is devoted here to outlining a proper quantitative model of the technique.

The imaging of an atom cloud can make use of the absorption or refractive index properties of the atoms. For absorptive imaging, spontaneous photon scattering by the atoms leaves a shadow imprint of the cloud on the probe beam: $I = I_0 e^{-D(\vec{r})}$. The optical depth $D(\vec{r})$ gives quantitative access to the density profile of the cloud integrated down the line of sight. There are a number of reasons why absorptive imaging is not particularly useful in-trap. Optical depths for on-resonant probe light ($D_0 \sim 10^2 - 10^3$) far exceed the limitations of imaging setups with a maximum observable optical depth of ~ 3 or so [120]. Detuning the probe from resonance to reduce the optical depth

only leads to another problem, image distortions due to lens-like refraction by the atom cloud [120]. From the perspective of non-destructiveness, the average recoil energy of an atom following spontaneous emission ($E_r \sim 45\text{nK}$ for ^{87}Rb) is comparable to the temperature of Bose-condensed samples and thus results in the loss of the atom from the condensate. Since sample sizes are small ($10^4 - 10^6$ atoms), obtaining an image with good signal-to-noise involves scattering a photon or more per atom. After a single absorption image a condensate will be mostly melted if not blown away.

The alternative to absorption imaging is to use an off-resonant phase-contrast technique sensitive to the phase shift induced by the cloud. A *nondestructive* image is possible because the spontaneous scattering rate Γ dies out more quickly away from resonance than the phase shift ξ . (For a probe detuned δ from resonance, $\Gamma \propto 1/\delta^2$ versus $\xi \propto 1/\delta$). The high on-resonant optical depth D_0 of a trapped condensate in particular allows for large probe detunings that significantly suppress spontaneous scattering while still maintaining a good imaging signal ($\xi \sim D_0/\delta \sim 1$). In the last part of this chapter, the “nondestructive” nature of phase-contrast imaging will be characterized in a little more detail, including the ultimate limit of a quantum nondemolition (QND) measurement for number.

2.2 Phase-contrast technique

To measure the phase shift induced by the atom cloud, an interference technique is needed. One way to do this would be to have an interferometer with the atom cloud in one arm. Phase-contrast imaging, which uses Fourier optics techniques, works in a very similar way. As shown in Figure 2.1, a probe laser beam detuned from resonance is incident on the atom cloud. The cloud acts as a phase object, diffracting (elastically scattering) some of the incident light. In analogy to the interferometer, the unscattered component forms the reference beam while the forward-scattered component carries the object information. The components are collected by an imaging lens and spatially

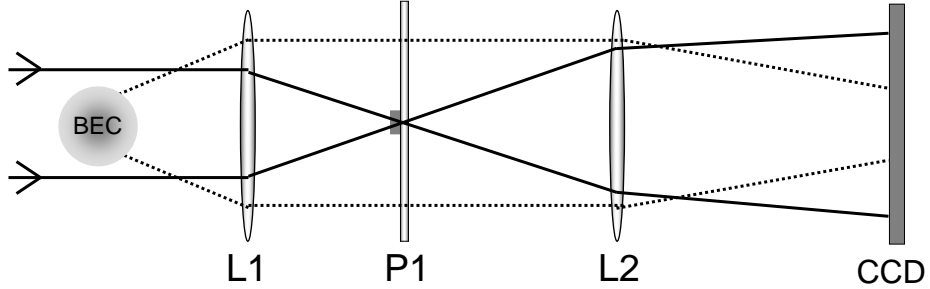


Figure 2.1: Phase-contrast imaging, using imaging lens L1, phase plate P1 in the back Fourier plane of L1 and magnification lens L2. A CCD records the images.

separated in the back focal plane due to the Fourier transforming effect of the lens [143]. This allows a small dielectric dot mounted on a glass substrate to selectively shift the phase of the unscattered component by ϕ_0 . A second magnification lens recombines the two light components, which interfere at the image plane to form a phase-contrast image of the atom cloud. A phase dot shift of $\phi_0 = \pi/2$ maximizes the contrast signal for small phase shifts.

The phase plate is a 1/16" thick, 1" diameter glass substrate with a small MgF_2 dot at the center of one face. The dot, with a diameter of $100\mu\text{m}$ and a thickness of $\lambda/4(n - 1) = 513\text{nm}$ corresponding to a phase shift of $\pi/2$, was deposited onto the substrate through a thin, stainless steel mask composed of a purchased optical pinhole. The opposite surface of the phase plate was then anti-reflection coated for 780nm to reduce fringes. An issue which arose in the deposition process was the crater-like appearance of the pinhole (due to the laser ablation used in its manufacture). In initial tests, the crater edges resulted in a non-uniform dot, presumably due to shadowing effects. This was solved by carefully polishing the thin steel around the hole to a flat finish.

The diameter of the dot was chosen based on typical condensate and probe beam sizes. The waist size for the probe beam incident on the atom cloud is 1mm compared to $30\mu\text{m}$ for the condensate radius; therefore, in the Fourier plane of the imaging

lens($f \sim 100\text{mm}$), the focused probe beam is $30\mu\text{m}$ compared with 1mm for the diffracted light. A $100\mu\text{m}$ diameter dot is large enough to include most of the focused probe beam, yet small enough to avoid significantly affecting the scattered light.

2.3 3-D imaging

There are a few points of interest relating to our imaging setup. The probe lasers for phase contrast are typically detuned up to several GHz from resonance. Furthermore, the detuning is changed often depending on the signal-to-noise and non-destructiveness desired. External cavity diode lasers with a DAVLL frequency lock [65] provide the versatility for probing both near and far from resonance. A Fabry-Perot cavity is rather useful to monitor the probe frequency relative to the well-defined frequency of a laser under saturation absorption lock [72].

To satisfy our insatiable desire for more and more information, three orthogonal axes of (nondestructive) imaging are simultaneously available to probe an atom cloud (see Fig. 2.2). The horizontal axes share a single CCD array, which is more than large enough to have side-by-side images of the atom cloud. The vertical imaging axis is integrated into an optical path normally occupied by one of the beams used for magneto-optical trapping [78]. As a result, some beam switching is required during the experimental cycle (see Fig. 2.2, side-view). All the complication of assembling a 3-D puzzle of extraordinarily dense optics around a fragile glass vacuum cell is well worth it, as each imaging direction has proven crucial to the vortex experiments discussed in subsequent chapters.

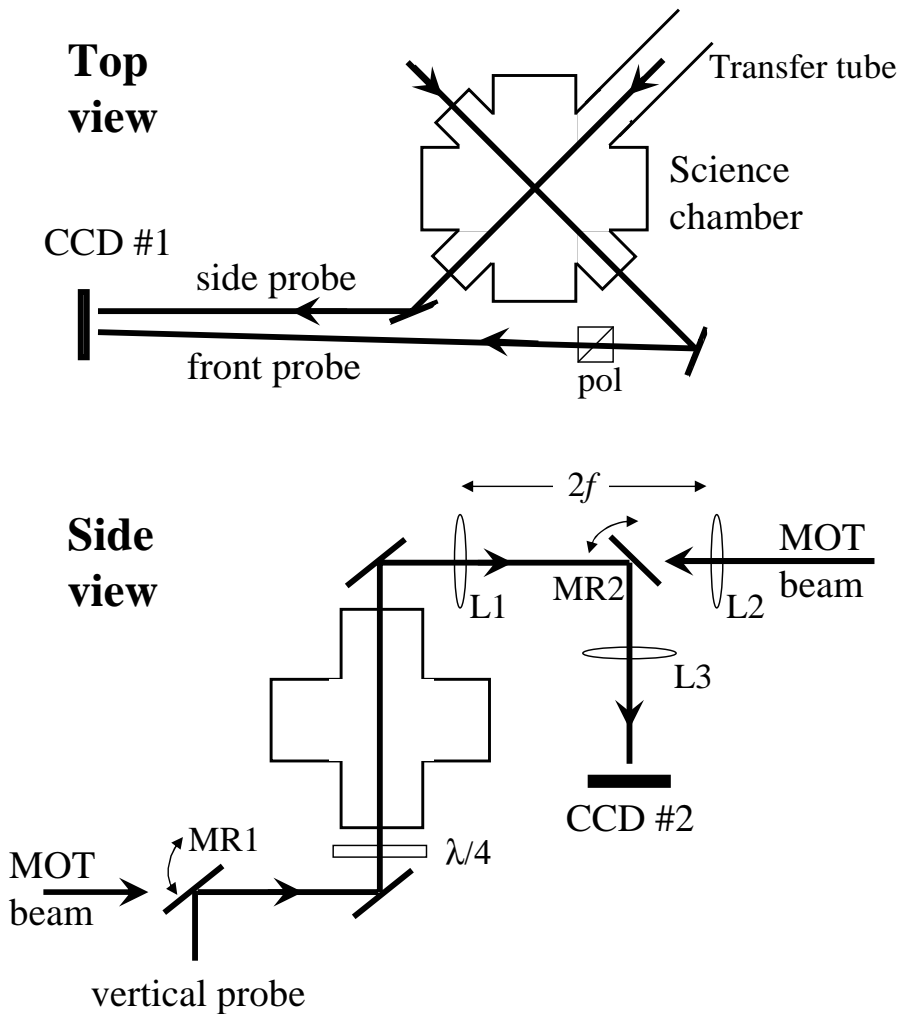


Figure 2.2: Experimental setup for 3-axis imaging. The top view shows the two horizontal imaging axes combined onto a single CCD camera. The more detailed side view shows the vertical axis, which is integrated into a MOT beam path. New Focus flipper mounts MR1 and MR2 rotate into place to permit imaging. Lenses L1 ($f = 120\text{mm}$) and L3 ($f = 700\text{mm}$) form the vertical imaging microscope. The matched pair of lenses L1 and L2 form a one-to-one telescope for the MOT beam.

2.4 Detailed calculation of imaging process

2.4.1 Overview of calculation

The purpose of this section is to provide a quantitative analysis of phase-contrast imaging, divided into the effect of the atom cloud (“object formation”), the optics (“image formation”), and image processing (“signal inversion”). The only real effort is to calculate the effect of probe laser propagation through the atomic cloud; the rest of the imaging system involves basic Fourier optics and is straight forward. Condensates as well as cold thermal clouds that are fairly dense can be imaged. For the purposes of imaging, a condensate is well approximated as a classical gas of independent quantum absorbers [126], in other words, a dielectric. Therefore, in order to understand object formation we simply need to calculate the refractive index and absorption for a generic atom cloud. The extra twist is that the magnetic confining potential for the atoms provides an ambient bias field that breaks the symmetry of the system. As in anisotropic crystals, the susceptibility of the atom cloud becomes a tensor quantity and the eigenmodes of propagation are no longer the simple free-space ones. As an additional complication, the TOP trap [78] used in this thesis work has a time-varying magnetic bias field which can be oriented in any direction in the horizontal plane. With three axes of imaging having three different polarizations constrained by optical access [Fig. 2.3], it is useful to investigate the effect of the bias field changing during a time-sequence of non-destructive pictures. Finally, in pushing the limits of imaging, for example in the analysis of the shape of an atom cloud, it is also useful to understand any nonlinear behaviour in phase-contrast imaging that will distort the image.

In calculating the optical response of an atom cloud, several references are useful [144, 143, 124] but the information is fairly scattered. Hopefully the expressions and techniques collected here will prove useful for other trapping experiments, including ones using absorption imaging.

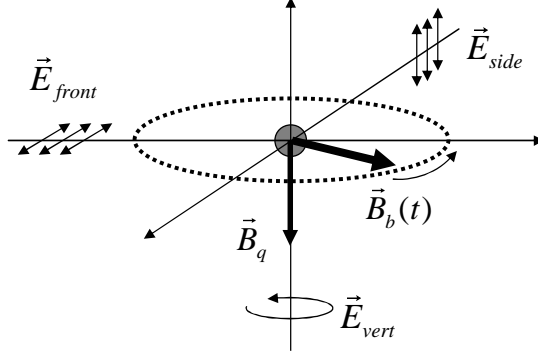


Figure 2.3: Probe polarizations for the three orthogonal axes of imaging. Also shown are the contributions to the magnetic bias field seen by atoms trapped in the TOP trap: (i) the rotating bias field B_b and (ii) a possible static component B_q depending on the position of the atoms in the quadrupole trap.

2.4.2 Atomic susceptibility

The starting point for light propagation in an atom cloud (“the medium”) is the Maxwell wave equation in a nonpermeable (zero magnetization) dielectric medium

$$\begin{aligned}\nabla^2 \vec{E} - \nabla(\nabla \cdot \vec{E}) - \mu_0 \frac{\partial^2 \vec{D}}{\partial t^2} &= 0 \\ \nabla \cdot \vec{D} &= 0\end{aligned}\tag{2.1}$$

where $\vec{D} = \epsilon_0 \vec{E} + \vec{\mathcal{P}}$ with $\vec{\mathcal{P}}$ being the induced polarization of the medium, \vec{E} the light’s electric field, and ϵ_0 and μ_0 the permittivity and permeability of free space respectively.

The polarization $\vec{\mathcal{P}}(\vec{r}, t)$ of an ultracold trapped cloud of atoms (including a condensate) is simply $n(\vec{r})\langle \vec{d} \rangle$, where $n(\vec{r})$ is the number density and $\langle \vec{d} \rangle = -\langle e\vec{r} \rangle$ is the induced dipole moment of a stationary atom in the presence of the probe laser field. Velocity effects are negligible for the trapped clouds in our experiment. Note that the spatial dependence of the polarization arises only from the density distribution.

We want to consider the optical probing of a ^{87}Rb cloud in a particular ground hyperfine state $5S_{1/2}|F, m_F\rangle$. Available transitions are the D1 and D2 lines reaching

the $5P_{1/2}$ and $5P_{3/2}$ electronic states respectively. We use the D2 line at $\lambda = 780\text{nm}$, with hyperfine structure resolved, as shown in Fig. 2.4. Contributions from all allowed transitions to the upper hyperfine manifold must be included when calculating the dipole response.

We focus on a single pair of states, labeled $\{|g\rangle, |e\rangle\}$ with associated resonant frequency ω_{eg} and linewidth γ . The state $|g\rangle$ ($|e\rangle$) is in the ground(excited) hyperfine manifold.

The incident probe laser with frequency ω has an electric field,

$$\vec{E}(\vec{r}, t) = \frac{\vec{E}}{2} e^{i\omega t - ik_0 z} + c.c. \quad (2.2)$$

The steady-state solution for probe durations $\tau \gg 1/\gamma$ is discussed in many places [124, 144]. In the dipole approximation ($e^{ik_0 z} \sim 1$) and the rotating wave approximation ($\omega - \omega_{eg} \ll \omega$), the dipole moment of an atom can be written as

$$\langle \hat{d}(t) \rangle = -\frac{i}{\hbar} \frac{\vec{d}_{ge} \cdot \vec{E}(t)}{\gamma/2 + i\delta_{eg}} \vec{d}_{eg} + c.c. \quad (2.3)$$

where $\delta_{eg} = \omega - \omega_{eg}$ is the detuning and \vec{d}_{eg} is the dipole matrix element $\langle e | \vec{d} | g \rangle$. Saturation effects [124] are justifiably ignored in phase-contrast imaging since probe detunings are many linewidths and probe intensities are low, typically $100 - 200 \mu\text{W}/\text{cm}^2$ compared to the saturation intensity $I_S = 1.6 \text{mW}/\text{cm}^2$ for Rubidium.

The main numerator dependence $(\vec{d} \cdot \vec{E}) \vec{d}$ of the dipole moment can be reordered as

$$(\vec{d}_{eg}^\dagger \vec{E}) \vec{d}_{eg} = \vec{d}_{eg} (\vec{d}_{eg}^\dagger \vec{E}) = (\vec{d}_{eg} \vec{d}_{eg}^\dagger) \vec{E} \quad (2.4)$$

where $\vec{d}_{eg} \vec{d}_{eg}^\dagger$ is a 3×3 (Hermitian) matrix (as opposed to $\vec{d}_{eg}^\dagger \vec{d}_{eg}$, which is a number). This allows us to write the polarization as $\vec{P} = \overleftrightarrow{\chi}_{eg} \vec{E}$ where the susceptibility $\overleftrightarrow{\chi}_{eg}$ is:

$$\overleftrightarrow{\chi}_{eg} = \frac{-i}{\hbar} \frac{\vec{d}_{eg} \vec{d}_{eg}^\dagger}{\gamma/2 + i\delta_{eg}} n(\vec{r}) \quad (2.5)$$

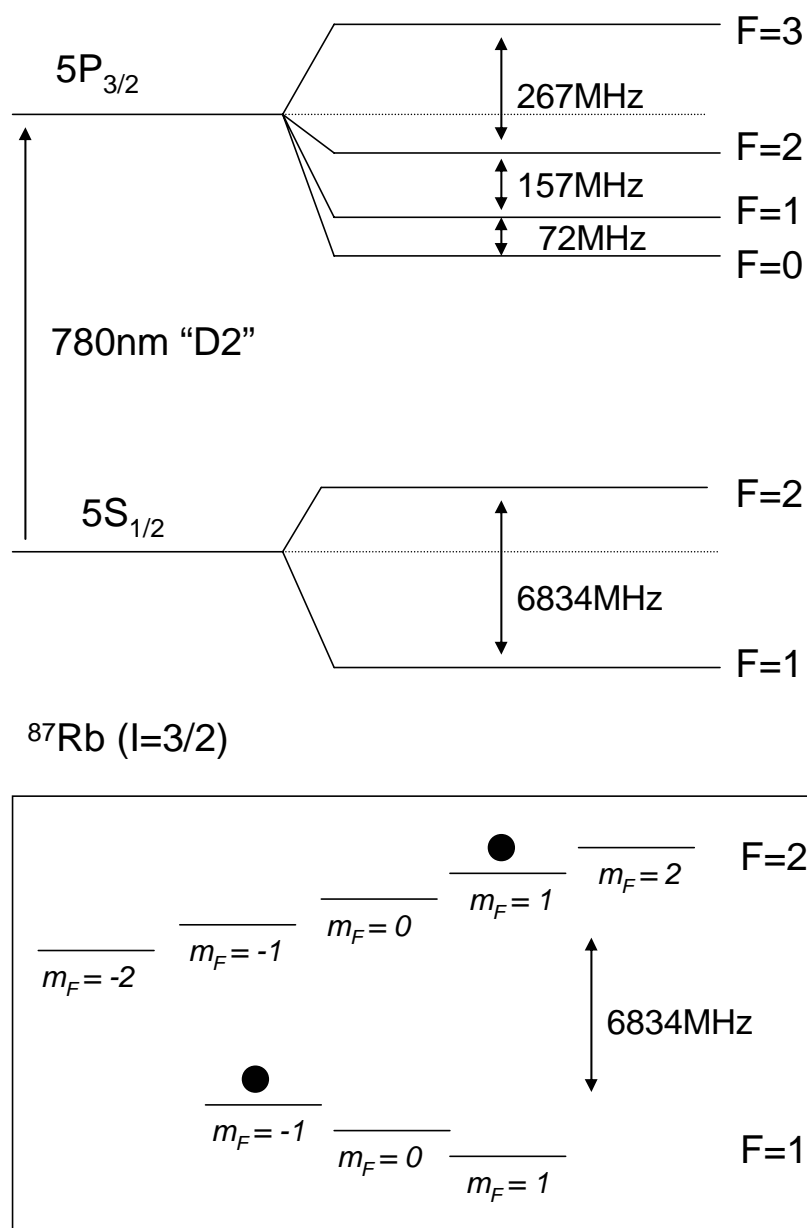


Figure 2.4: Relevant ^{87}Rb level structure showing the D2 optical transition with ground and excited hyperfine manifolds resolved. Also shown in the boxed region is the Zeeman sub-structure for the ground hyperfine states with filled circles identifying the two magnetically trapped states used in the experiment.

To include all hyperfine states $|e\rangle \in |F', m_{F'}\rangle$ in the upper manifold, we sum up their contributions $\overleftrightarrow{\chi}_{eg}$ to the total susceptibility. The dipole decay rate from the upper hyperfine states is γ , independent of $m_{F'}$ sublevel; therefore, the excited state dependence in $\overleftrightarrow{\chi}_{eg}$ is through the detuning and dipole matrix $\vec{d}_{eg}\vec{d}_{eg}^\dagger$ only.

It is very useful to define a dipole matrix normalized to the cycling transition matrix element as follows:

$$\overleftrightarrow{C}(e, g) = \frac{\vec{d}_{eg}\vec{d}_{eg}^\dagger}{|\vec{d}_{cyc}|^2} \quad (2.6)$$

Thus the net expression for the susceptibility of an atom cloud in ground hyperfine state $|g\rangle$ is:

$$\overleftrightarrow{\chi} = -i \sum_{e \in \{F', m_{F'}\}} \frac{n\sigma}{k_0} \frac{\overleftrightarrow{C}(e, g)}{1 + i \frac{2\delta_{eg}}{\gamma}} \quad (2.7)$$

where the sum is over all excited states $\{|e\rangle\}$. If more than one ground state is occupied, the susceptibility should also be averaged over all of them. The value of σ is the standard crosssection for a cycling transition

$$\sigma = \frac{3\lambda^2}{2\pi} \quad (2.8)$$

In obtaining Eqn. 2.7, the standard relation for the linewidth of a cycling transition was also used

$$\gamma = \frac{\omega^3 |\vec{d}_{cyc}|^2}{3\pi\epsilon_0 \hbar c^3} \quad (2.9)$$

We could express the susceptibility tensor in Cartesian co-ordinates; however, the natural basis to use is the spherical tensor one defined as:

$$\hat{e}_\pm = \mp \frac{1}{\sqrt{2}}(\hat{x} \pm i\hat{y}), \quad \hat{e}_0 = \hat{z} \quad (2.10)$$

If we further choose to use ‘‘atom co-ordinates’’, where the direction of the magnetic bias field lies along the \hat{z} -axis, then dipole selection rules cause the $\overleftrightarrow{C}(e, g)$ matrix [Eqn. 2.6] to be diagonal for each of the terms in the susceptibility sum [Eqn. 2.7]. The total

susceptibility is, as a result, also diagonal in this basis with value:

$$\overleftrightarrow{\chi} = \begin{pmatrix} \chi_+ & 0 & 0 \\ 0 & \chi_0 & 0 \\ 0 & 0 & \chi_- \end{pmatrix} \quad (2.11)$$

where

$$\chi_q = -i \sum_{e \in \{F', m_{F'}\}} \frac{n\sigma}{k_0} \frac{c_q(e, g)}{1 + i \frac{2\delta_{eg}}{\gamma}} \quad (2.12)$$

The Clebsch-Gordan type terms $c_q(e, g)$ are the diagonal elements of $\overleftrightarrow{C}(e, g)$ in the atom basis [124]:

$$\begin{aligned} c_q(F, m_F; F', m_{F'}) &= \frac{1}{N} \frac{|\hat{\epsilon}_q \cdot \vec{d}_{eg}|^2}{|\vec{d}_{cyc}|^2} \\ &= \frac{1}{N} (2J+1)(2J'+1)(2F+1)(2F'+1) \\ &\quad \times \left| \begin{Bmatrix} L' & J' & S \\ J & L & 1 \end{Bmatrix} \begin{Bmatrix} J' & F' & I \\ F & J & 1 \end{Bmatrix} \begin{pmatrix} F & 1 & F' \\ m_F & q & -m_{F'} \end{pmatrix} \right|^2 \end{aligned} \quad (2.13)$$

The curly-(round-)bracketed terms are 6-j (3-j) symbols, easily evaluated in Mathematica for example. The normalization N is chosen such that $c_q = 1$ for the cycling transition, namely $|2, 2\rangle \rightarrow |3, 3\rangle$ for ^{87}Rb . The normalized values for the D2 line of ^{87}Rb ($I=3/2$) can be found listed in a previous thesis [120].

The contribution from each transition to the susceptibility in Eqn. 2.12 may be written as the sum of a real and imaginary part, $\chi'_q(e, g) + i\chi''_q(e, g)$ with values:

$$\begin{aligned} \chi'_q(e, g) &= \frac{2\delta_{eg}}{\gamma} \chi''_q(e, g) \\ \chi''_q(e, g) &= -\frac{n\sigma}{k_0} \frac{c_q(e, g)}{1 + \left(\frac{2\delta_{eg}}{\gamma}\right)^2} \end{aligned} \quad (2.14)$$

where the imaginary part is responsible for absorption and the real part for the refractive index. Clearly for large detunings ($\delta_{eg} \gg \gamma$) the real part dominates.

2.4.3 Object formation

With the polarizability in hand, we can proceed with the effect of light propagation through the atom cloud. Returning to the wave equation [Eqn. 2.1] and assuming a probe laser frequency ω , we obtain an equation for the laser's electric field $\vec{E}(\vec{r})$ inside the medium:

$$\nabla^2 \vec{E} - \nabla(\nabla \cdot \vec{E}) + k^2 \frac{\overleftrightarrow{\epsilon}}{\epsilon_0} \vec{E} = 0 \quad (2.15)$$

where

$$\overleftrightarrow{\epsilon} = \epsilon_0(1 + \overleftrightarrow{\chi}) \quad (2.16)$$

First, diffraction effects in the atom cloud are neglected, which amounts to dropping all transverse derivatives and keeping only those with respect to the propagation (\hat{z} -)direction. To estimate the magnitude of diffraction effects we can use ray-optics and treat the cloud as a sphere of radius R and uniform refractive index. Then the transverse deviation of rays within the cloud is roughly $\Delta x \sim \xi \lambda$ where ξ is the peak phase shift of the probe through the cloud. Typically $\xi \lesssim 1$, so diffraction effects within the cloud do not exceed the imaging resolution ($\gtrsim \lambda$) and are unimportant.

Further, the density of the atom cloud is also assumed to change slowly compared to λ . The laser field can then be approximated as $\vec{E} = \vec{A}(\vec{r})e^{-ik_0z}$ where $\vec{A}(\vec{r})$ is slowly varying. Called the paraxial or WKB approximation, this amounts to neglecting reflection by the medium [143].

Incorporating these approximations into the wave equation Eqn. 2.15 and working in the atom co-ordinates where $\overleftrightarrow{\chi}$ (or $\overleftrightarrow{\epsilon}$) is diagonal, we can readily solve for two eigenmodes of propagation $\{\vec{E}_a, \vec{E}_b\}$ in the medium, namely

$$\vec{E}_i(\vec{r}) = \vec{E}'_i(\vec{r})e^{-i \int^z k_i(\vec{r}') dz'}, i \in \{a, b\} \quad (2.17)$$

which satisfy the eigenvalue problem,

$$\left(k_0^2 \frac{\overleftrightarrow{\epsilon}(\vec{r})}{\epsilon_0} - k^2(1 - \hat{z}\hat{z}^\dagger) \right) \vec{E} = 0 \quad (2.18)$$

The spatially dependent eigenvalues $k_{a,b}(\vec{r})$ are determined from a generalized Fresnel equation [143] for a spatially dependent anisotropic medium,

$$\sum_q \frac{|z_q|^2(1 + \chi_q(\vec{r}))}{(1 + \chi_q(\vec{r})) - \frac{k^2}{k_0^2}} = 0 \quad (2.19)$$

where the components χ_q of the susceptibility in the atom frame have already been determined [Eqn. 2.12]. The only difficulty to solving these equations is to calculate the vector components z_q of the propagation direction in terms of the atom-frame spherical co-ordinates. If the magnetic bias field has polar co-ordinates $\{\theta, \phi\}$ with respect to the propagation direction [Figure 2.5], then the transformation from lab to atom co-ordinates is achieved with the rotation operator $\mathcal{D}(\theta, \phi) = \mathcal{D}_y(-\theta)\mathcal{D}_z(-\phi)$ in $l = 1$ representation

$$\mathcal{D}(\theta, \phi) = \begin{pmatrix} \frac{1}{2}e^{i\phi}(1 + \cos \theta) & \frac{1}{\sqrt{2}}\sin \theta & \frac{1}{2}e^{-i\phi}(1 - \cos \theta) \\ -\frac{1}{\sqrt{2}}e^{i\phi}\sin \theta & \cos \theta & \frac{1}{\sqrt{2}}e^{-i\phi}\sin \theta \\ \frac{1}{2}e^{i\phi}(1 - \cos \theta) & -\frac{1}{\sqrt{2}}\sin \theta & \frac{1}{2}e^{-i\phi}(1 + \cos \theta) \end{pmatrix} \quad (2.20)$$

so that the z-direction in the atom co-ordinates used in equations (2.18) and (2.19) is

$$\hat{z} = \begin{pmatrix} \frac{1}{\sqrt{2}}\sin \theta \\ \cos \theta \\ -\frac{1}{\sqrt{2}}\sin \theta \end{pmatrix} \quad (2.21)$$

Since the \hat{z} components depend only on θ , the same is true of the wavevector and eigenmodes in the atom co-ordinates. The ϕ dependence arises when the eigenvectors are transformed back to the lab co-ordinates with $\mathcal{D}^\dagger(\theta, \phi)$.

Equations (2.17)-(2.21) provide the total solution to propagation in the medium. A probe laser, \vec{E}_{in} , is incident on the atom cloud where \vec{E}_{in} is some superposition of the free-space circular polarization basis,

$$\vec{E}_{in} = \begin{pmatrix} E_+ \\ 0 \\ E_- \end{pmatrix} \quad (2.22)$$

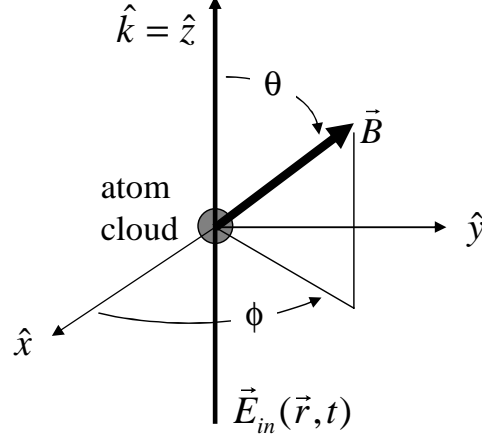


Figure 2.5: Magnetic bias field orientation relative to probe propagation direction $\hat{k} = \hat{z}$.

The output laser field \vec{E}_{out} is obtained as follows:

- 1) Project \vec{E}_{in} onto the free-space limit of the medium's eigenvectors, which are in lab co-ordinates:

$$\lim_{n \rightarrow 0} (\mathcal{D}^\dagger(\theta, \phi) \vec{E}_i) = \begin{pmatrix} E_{i+} \\ 0 \\ E_{i-} \end{pmatrix}, i \in \{a, b\} \quad (2.23)$$

where $|\vec{E}_i|^2 = 1$ and \mathcal{D} is given in Eqn. 2.20.

- 2) Apply phase shift and absorption to each of the eigenmodes.
- 3) Reproject (if necessary) onto the free-space circular basis.

In summary, long after the medium we have:

$$\vec{E}_{out} = (P^\dagger M P) \vec{E}_{in} \quad (2.24)$$

where P is the projection onto the free-space limit of the eigenvectors [Eqn. 2.23] and can be written generally in terms of angles $\{\alpha, \beta\}$

$$P = \begin{pmatrix} E_{a+} & 0 & E_{a-} \\ 0 & 0 & 0 \\ E_{b+} & 0 & E_{b-} \end{pmatrix} \equiv \begin{pmatrix} e^{-i\alpha/2} \cos \beta & 0 & -e^{i\alpha/2} \sin \beta \\ 0 & 0 & 0 \\ e^{-i\alpha/2} \sin \beta & 0 & e^{i\alpha/2} \cos \beta \end{pmatrix} \quad (2.25)$$

M gives the effect of propagation through the medium:

$$M = \begin{pmatrix} e^{-i\xi_a} & 0 & 0 \\ 0 & 0 & 0 \\ 0 & 0 & e^{-i\xi_b} \end{pmatrix} \quad (2.26)$$

with $\xi_{a,b} = \int_{-\infty}^{\infty} (k_{a,b}(\vec{r}) - k_0) dz$. The real (imaginary) part of ξ describes the phase shift (absorption) acquired by a probe passing through the cloud.

Although the equations 2.17 & 2.18 for \vec{E}_i and k_i are straightforward to solve, the final expressions in general involve all of the susceptibility matrix elements as well as the angles θ and ϕ . The solutions are too complicated to be written out here; however, a relatively useful expression for the eigenvalues themselves is shown here for the case where the susceptibility is small:

$$k_{a,b} = k_{av} \pm \frac{\delta k}{2} \quad (2.27)$$

$$\frac{k_{av}}{k_0} \approx 1 + \frac{1}{16} \{ 3\chi_+ + 3\chi_- + 2\chi_0 + \cos(2\theta)(\chi_+ + \chi_- - 2\chi_0) \}$$

$$\frac{\delta k}{k_0} \approx \frac{1}{8} \{ 9\chi_+^2 + 4\chi_0^2 - 4\chi_0\chi_- + 9\chi_-^2 - 2\chi_+(2\chi_0 + 7\chi_-) \\ + 2\cos(2\theta)(3\chi_+ - 2\chi_0 - \chi_-)(\chi_+ + 2\chi_0 - 3\chi_-) \\ + \cos^2(2\theta)(\chi_+ - 2\chi_0 + \chi_-)^2 \}^{\frac{1}{2}}$$

To get a feeling for the size of the susceptibility under typical experimental conditions, we can consider the simple situation of the bias field aligned with the propagation axis of the probe laser. In this case the eigenmodes in the medium are the two circular polarizations with wavevectors $k_{a,b} = k_0\sqrt{1 + \chi_{\pm}} \sim k_0(1 + \chi_{\pm}/2)$ for small χ_q . If we focus on a single transition for one of the polarizations, say \hat{e}_+ , then the susceptibility χ_+ can be written as

$$\chi_+ \sim -\frac{D_{pk}}{k_0 R} \frac{\gamma}{2\delta} \left(1 + i\frac{\gamma}{2\delta} \right), \quad \delta \gg \gamma \quad (2.28)$$

where $D_{pk} \sim n_0\sigma R$ is the peak on-resonant optical depth (absorption coefficient), n_0 the peak atom density, and R the radius of the cloud. Typical experimental parameters

for a condensate in-trap are 10^6 atoms, $R \sim 28\mu\text{m}$ and $D_{pk} \sim 300$; therefore χ_+ will be small ($\lesssim 0.1$) for $\delta \gtrsim 5\gamma \sim 30\text{MHz}$. For comparison, typical probe detunings in the experiment are 100MHz or more from the nearest resonance.

Since the peak phase shift of the probe is $\phi_{pk} = \frac{D_{pk}}{2} \frac{\gamma}{2\delta}$ for a single transition, the susceptibility can perhaps more usefully be written as

$$\chi_+ \sim -\frac{2\phi_{pk}}{k_0 R} \left(1 + i \frac{\gamma}{2\delta}\right), \quad \delta \gg \gamma \quad (2.29)$$

Sufficient signal-to-noise is achieved in images of atom clouds for peak phase shifts of ~ 0.5 , a typical value for the experiment. Under these circumstances, for a condensate with radius $R \geq 20\mu\text{m}$, the magnitude of χ is less than 0.01, certainly small.

2.4.4 Phase-contrast image formation

After propagation through the atom cloud, the probe laser is the sum of scattered and unscattered field components, approximately identified as follows:

$$\vec{E}_{out} = \underbrace{\vec{E}_{in}}_{unscattered} + \underbrace{(\vec{E}_{out} - \vec{E}_{in})}_{scattered} \quad (2.30)$$

The unscattered part is quite reasonably approximated by the incident field \vec{E}_{in} since the laser beam profile (with waist $w \sim 1\text{mm}$) is typically much larger than the cloud (with radius $R \sim 28\mu\text{m}$), making the fraction of scattered power ($\propto R^2/w^2 \ll 1$) small.

As mentioned above, the spatial Fourier transformation performed by the imaging lens [Fig. 2.1] spatially separates the light field into its unscattered and scattered components with, crudely speaking, zero and non-zero spatial frequencies respectively. This allows a small phase dot in the back Fourier plane of the imaging lens to selectively shift the phase of the unscattered component by ϕ_0 . Thus, after the remainder of propagation to the image plane, the total probe laser field is:

$$\begin{aligned} \vec{E}_{image}(x, y) &= e^{i\phi_0} \vec{E}_{in} + (\vec{E}_{out} - \vec{E}_{in}) \\ &= \left[(e^{i\phi_0} - 1) + P^\dagger M P \right] \vec{E}_{in} \end{aligned} \quad (2.31)$$

using the expression for \vec{E}_{out} from Eqn. 2.24. Any magnification m in the imaging system has been omitted here but can easily be included in this and subsequent formulae by adjusting the coordinates according to $\{x, y\} \rightarrow \{mx, my\}$.

In the experiment, a CCD camera collects the image proportional to the incident intensity ($I \propto |\vec{E}_{image}|^2$). For a given atom cloud, the standard protocol [78, 120] actually involves a sequence of three images, a probe shot to obtain the intensity profile $I(\vec{r})$ of the probe laser modulated by the presence of the atom cloud, a normalization shot to obtain the intensity profile $I_0(\vec{r})$ of the probe alone, and finally a background shot without probe light, giving $I_{backgr}(\vec{r})$. The normalization shot can be realized either by first destroying the condensate or, more nondestructively, by detuning the probe sufficiently far from resonance. On a pixel-by-pixel basis, background subtraction and normalization are performed to yield the raw phase-contrast signal:

$$S(\vec{r}) = \frac{I(\vec{r}) - I_{backgr}(\vec{r})}{I_0(\vec{r}) - I_{backgr}(\vec{r})} - 1 \quad (2.32)$$

2.4.5 Phase-contrast signal inversion

The final step of imaging is to invert the raw signal S [Eqn. 2.32] for the column density of the atom cloud on a pixel-by-pixel basis. This step requires knowledge of the exact form of S , which in general depends on the details of the imaging setup such as the probe polarization, magnetic bias field orientation and so on. It is most to the point to consider the specific situations arising in the apparatus.

A variety of constraints on the optical table have resulted in the following arrangements for the three different orthogonal probe directions [see Figs. 2.2 & 2.3]. The “front” horizontal axis uses a probe laser incident with horizontal, linear polarization. Additionally, a horizontally polarizing beamsplitter cube is situated in front of the camera. The “side” horizontal axis uses a vertically polarized probe incident on the atoms. Lastly, the vertical axis uses circular polarization. In all cases, the rotating magnetic

bias field of the TOP trap may have an arbitrary orientation in the horizontal plane at the time of imaging.

To calculate the phase-contrast signal, the detuning of the probe laser from all resonances is assumed to be large enough that the imaginary part of the susceptibility can be disregarded [see Eqn. 2.14]. Under this approximation, the probe eigenmodes in the atom frame are real as are their wavevectors. A useful way to obtain the phase-contrast signal starts with Eqn. 2.31 for \vec{E}_{image} and uses the general expression Eqn. 2.25 for the projection matrix P in terms of angles α and β . Both angles depend on the magnetic bias field orientation through $\alpha = 2\phi$ and $\beta = \beta(\theta)$. The net signal for the front axis, for example, is

$$\begin{aligned}
S_{front}(\xi_{av}, \delta\xi) &= 4 \sin \frac{\phi_0}{2} \left[\sin \frac{\phi_0}{2} + \cos \frac{\delta\xi}{2} \sin \left(\xi_{av} - \frac{\phi_0}{2} \right) \right] \\
&+ 4 \sin \frac{\phi_0}{2} \left[\cos \alpha \sin 2\beta \cos \left(\xi_{av} - \frac{\phi_0}{2} \right) \sin \frac{\delta\xi}{2} \right] \\
&- \frac{1}{4} [3 - \cos 2\alpha + 2 \cos^2 \alpha \cos 4\beta] \sin^2 \frac{\delta\xi}{2}
\end{aligned} \tag{2.33}$$

in which ϕ_0 is the phase shift due to the phase dot, and ξ_{av} and $\delta\xi$ are the phase shifts due to the atom cloud in terms of wavevectors k_{av} and δk [Eqn. 2.27]:

$$\begin{aligned}
\xi_{av}(x, y) &= \int_{-\infty}^{\infty} (k_{av}(\vec{r}) - k_0) dz \\
\delta\xi(x, y) &= \int_{-\infty}^{\infty} (\delta k(\vec{r}) - k_0) dz
\end{aligned} \tag{2.34}$$

Physically, ξ_{av} is the average phase shift of the probe passing through the cloud while $\delta\xi$ is indicative of Faraday rotation of the probe's polarization. Both quantities are directly proportional to the column density of the atom cloud integrated along the probe line of sight and have implicit dependencies on the bias field orientation through the polar angle θ (see Eqn. 2.27).

Phase-contrast signals such as S_{front} of Eqn. 2.33 cannot in general be algebraically inverted for the column density. However, a main point of this section is to demonstrate that, when phase shifts are not too large ($\xi_{av} \sim \delta\xi \lesssim 1$), all the probe

signals can be reasonably approximated by the simple result

$$\begin{aligned}
 S_0(\xi) &= 4 \sin \frac{\phi_0}{2} \left[\sin \frac{\phi_0}{2} + \sin \left(\xi - \frac{\phi_0}{2} \right) \right] \\
 \xi &= \begin{cases} \xi_{av} & \text{front, side probe} \\ \xi_{av} + \eta \delta \xi & \text{vertical probe} \end{cases} \quad (2.35)
 \end{aligned}$$

where $\eta = 0(\pm 1)$ applies to a strong(weak) trapping potential (see below). The approximate signal is the same expression one would obtain for a *scalar* probe field. For the case of a linearly polarized probe laser such as the front axis, this amounts to neglecting Faraday rotation effects, which can be seen directly by setting $\delta \xi = 0$ in the expression for the front probe signal [Eqn. 2.33]. A nice feature of $S_0(\xi)$ is that it can be readily inverted for ξ

$$\xi = \arcsin \left[\frac{S_0}{4 \sin \frac{\phi_0}{2}} - \sin \frac{\phi_0}{2} \right] + \frac{\phi_0}{2} \quad (2.36)$$

Eqn. 2.36 is the signal inversion used in the experiment with S_0 replaced by the actual acquired signal. In order to assess the validity of this approximation, as well as other effects such as bias field orientation, a representative example is now studied in numerical detail. The full phase-contrast signal S_{front} [Eqn. 2.33] for the front probe axis is calculated for a condensate under typical experimental conditions and compared to the approximate expression S_0 [Eqn. 2.35]. The magnetically trapped ground hyperfine state, $|F = 1, m_F = -1\rangle$, is considered. In addition, the two typical configurations of the TOP trap are assessed, (i) a strong trap and (ii) a weak trap where the atom cloud sags downward by about 1mm under the pull of gravity. In the former case the atoms feel a bias field B_b rotating in the horizontal plane. In the later sagged case, the atoms feel both a rotating field of $B_b \sim 1.7\text{G}$ and an additional static downward field of $B_q \sim 3.2\text{G}$. Relevant condensate parameters for the weak trap include number $N \sim 10^6$ and Thomas-Fermi radius $R \sim 28\mu\text{m}$, giving a peak on-resonant optical depth of $D_{pk} \sim 300$, assuming a cycling transition. The same optical depth is used for the

strong trap for comparison purposes.

First, a feeling for the size of the optical phase shifts induced by the condensate (in the weak trap) is given in Fig. 2.6 where ξ_{av} and $\delta\xi$ are plotted over the standard range of probe detunings used. The probe is detuned below all resonances for the $|1, -1\rangle$ state such that the signal is positive or bright on the CCD screen relative to the background. The typical peak phase shift of $|\xi_{av}| \sim 0.3 - 0.5$, which sets the standard range of detunings, represents an operational compromise between nondestructiveness and a good signal-to-noise ratio [see Section 2.5].

Figure 2.7(a) shows the dependence of ξ_{av} and $\delta\xi$ on the orientation of the rotating bias field B_b for the $|F = 1, m_F = -1\rangle$ state and a fixed detuning. The fractional peak-to-peak variation of ξ_{av} is fairly small whereas the value of $\delta\xi$ varies considerably over bias orientation. The variation of the phase-contrast signal itself is shown in Figs. 2.7(b)&(c) for a variety of peak average phase shifts. The *fractional* variation becomes worse when the phase shift is larger or, most importantly, when the probe frequency approaches a resonance, the nearest one corresponding to the $F = 1 \rightarrow F' = 0$ transition at the right edge of the plots in Fig. 2.7. Additionally, the strong trap shows more of an effect than the weak one. By way of conclusion, in the weak trap where most of the vortex work is pursued, reasonable phase shifts $\xi_{av} \leq 0.6$ and probe frequencies greater than 100MHz from resonance will ensure that variations in the peak signal will not exceed 5% if the bias field orientation is left uncontrolled. A more serious problem will arise for samples of smaller number, which force the probe detuning near to resonance to achieve a good signal.

Another important imaging effect to consider is nonlinearity in the phase contrast signal, which if left unaccounted for, will effectively distort the image of an atom cloud, making it more “peaky” or flat-topped depending on the trend of the nonlinearity. Since we use only an approximate form of the true signal to invert for an image, there is the potential for distortions due to nonlinearity. The maximum fractional difference between

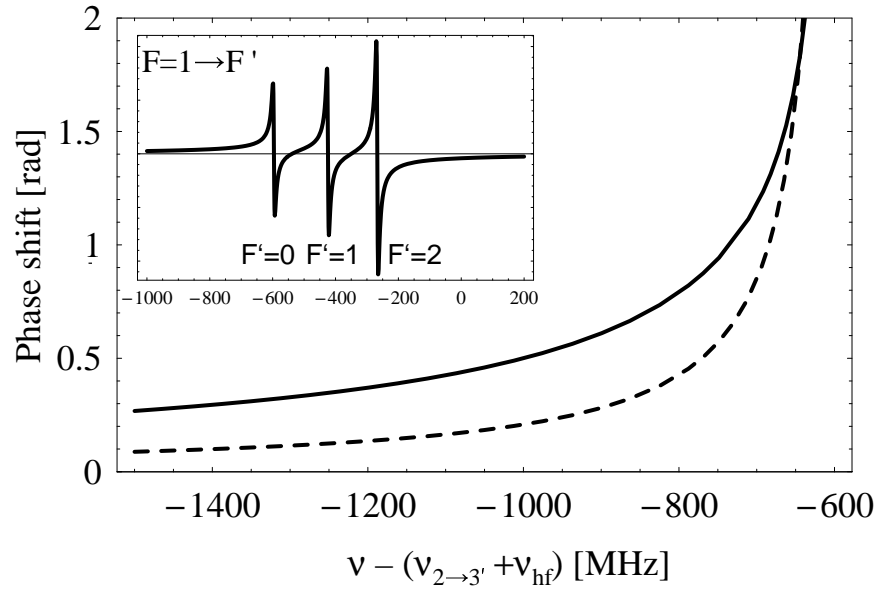


Figure 2.6: Average phase shift ξ_{av} (solid line) and differential phase shift $\delta\xi$ (dashed line) induced by a typical $|F = 1, m_F = -1\rangle$ condensate versus probe laser frequency ν . The frequency range plotted is the usual operating range in the experiment. The inset shows the average phase shift over a larger frequency range including all resonances.

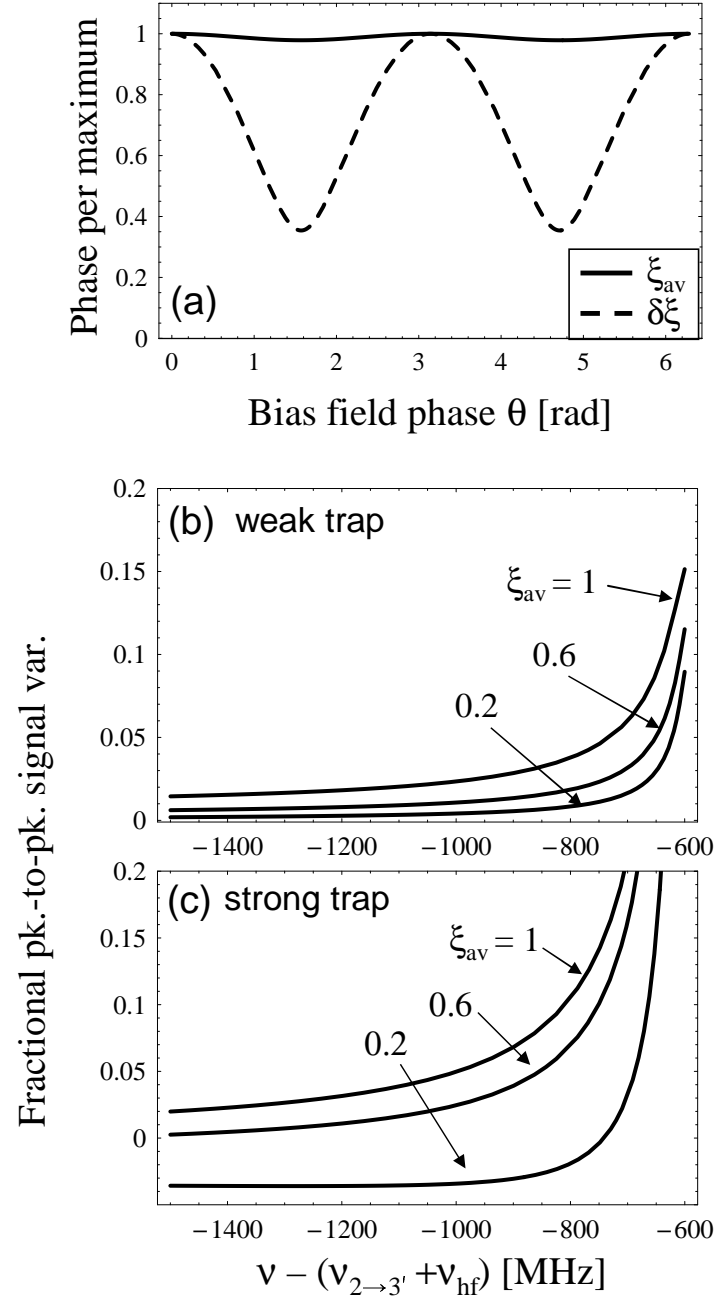


Figure 2.7: (a)Phase variation due to rotating TOP bias field $\vec{B}_b(\theta)$. Total fractional variation of phase-contrast signal is shown in (b) and (c) as a function of probe frequency ν for three different magnitudes of the average optical phase shift ξ_{av} .

the approximate signal $S_0(\xi_{av})$ [Eqn. 2.35] and the front probe signal $S_{front}(\xi_{av}, \delta\xi)$ [Eqn. 2.33] is shown in Fig. 2.8, again for the $|1, -1\rangle$ state over typical detunings. The strong trap shows more of an effect than the weak one. As a rule of thumb, an effect exceeding 10% should only arise for samples of small number where the probe needs to be less than 100MHz detuned of the $F = 1 \rightarrow F' = 0$ resonance to achieve a good signal ($\xi_{av} \sim 0.5$).

There is one additional nonlinear effect called “phase wrap,” which is intrinsic to phase contrast. Since the signal is an interference effect with 2π periodicity, the signal must saturate for large enough phase shifts and begin to decrease [see Fig. 2.9]. The saturation point depends on the choice of phase dot retardance. For the choice of $\phi_0 = \pi/2$ used in the experiment, the effect is not much of an issue for *positive* phase shifts as the saturation point occurs at a fairly high phase shift. However, it is an issue for negative phase shifts since the phase-contrast signal is not symmetric. This is the main reason why the probe detuning is chosen to give a positive phase shift when looking at a cloud composed of a single spin state.

2.5 Nondestructive imaging

The utility of phase-contrast imaging lies in its nondestructive character, allowing time sequences of images or “movies” to be taken of a single atom cloud in-trap. This is particularly valuable for measuring time-dependent excitations of a condensate with a minimum amount of data-taking [e.g. Section 3.6]. As well, nondestructive imaging can provide the only way to analyze condensate dynamics in situations when the initial conditions fluctuate from each realization of a condensate sample to the next [e.g. Section 3.5]. A potentially interesting application of phase-contrast imaging would be to use the information garnered from an image to feed back onto the condensate, perhaps for some type of coherent control. Admittedly, a servo-loop based on the current implementation of the imaging would have a fairly low bandwidth since

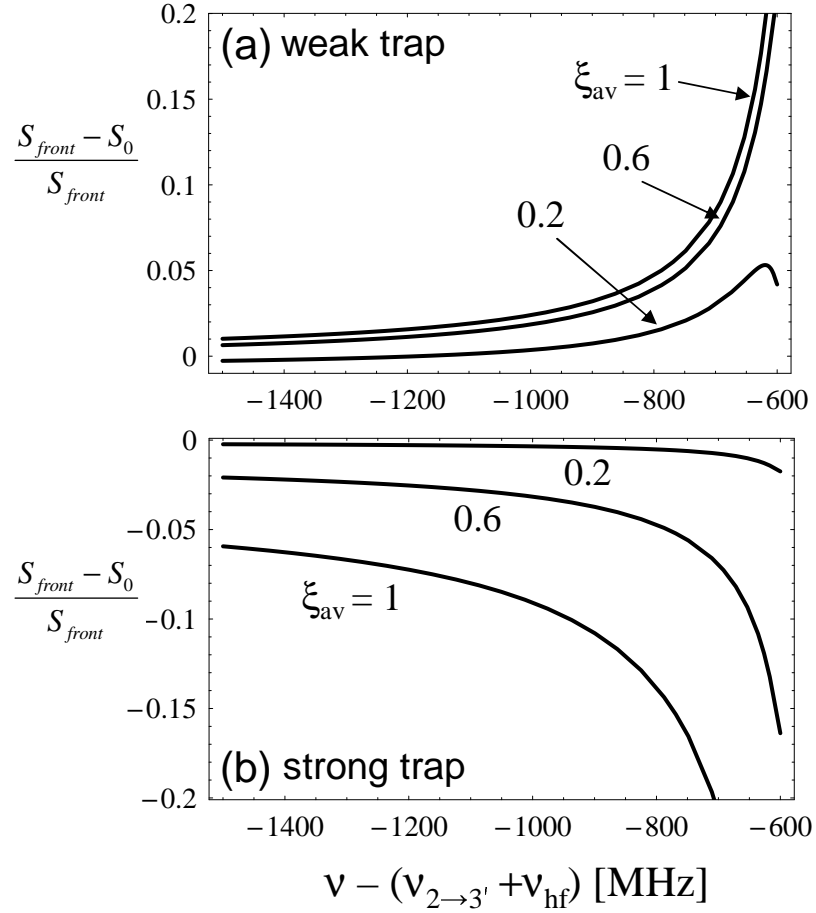


Figure 2.8: Fractional error between approximate and true phase-contrast signals, S_0 and S_{front} respectively, for the front probe direction as a function of probe laser frequency ν . Contours of fixed optical phase shift ξ_{av} are labeled accordingly. Overlapping contours would indicate a linear error independent of phase shift. The degree of image nonlinearity accrued by using the approximate signal for image processing can be inferred from the vertical spread of the contours at a fixed probe frequency ν .

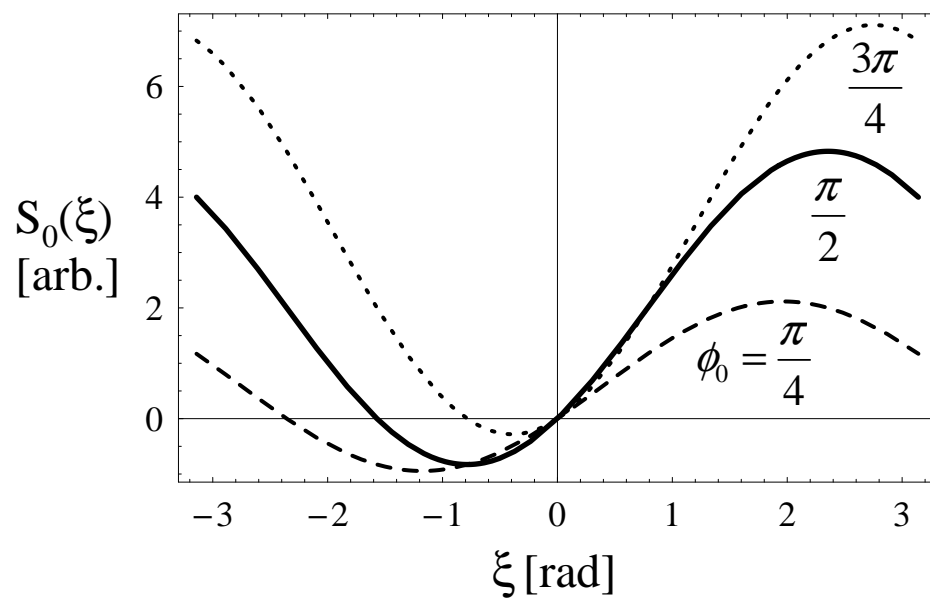


Figure 2.9: Phase-contrast signal S_0 as a function of induced optical phase shift ξ for three different phase dot retardances ϕ_0 . The experiment uses $\phi_0 = \pi/2$

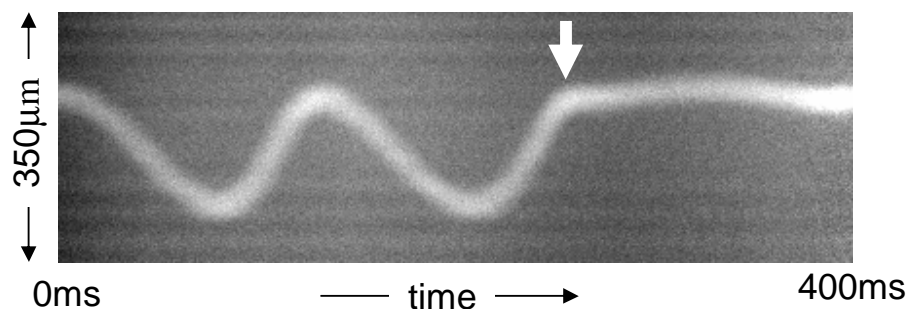


Figure 2.10: Nondestructive streak-camera image of a trapped condensate showing removal of its center-of-mass motion (up-down oscillation) by shifting the trap. The arrow indicates the time where the trap center is suddenly shifted.

the readout and processing of a sequence of images from the CCD camera requires a reasonable fraction of a second. As a simple example, phase contrast can be useful to assess and remove undesirable center-of-mass oscillations (“slosh”) of the condensate in the confining potential. Sloshing represents a hindrance in many experiments such as wavefunction engineering [Chapter 3], where the condensate needs to be selectively manipulated across its spatial extent. For the simple case of reproducible slosh from shot to shot, a phase-contrast image can be made at the start of the day to measure the oscillations. In subsequent shots, an “antislosh” step can be applied, where the trap center is suddenly kicked or shifted with the correct phase and amplitude to bring the condensate to a stop [Fig. 2.10].

The statement that phase-contrast imaging is “nondestructive” is not an exact statement and requires some quantitative clarification. The two issues focused on here are (i) condensate depletion and heating due to residual spontaneous scattering from the off-resonant probe laser and (ii) the effect on condensate phase due to the laser-induced ac Stark shift.

2.5.1 Spontaneous scattering and number loss

The nondestructive character of phase-contrast imaging is intimately related to the signal-to-noise desired for the images. A discussion of signal-to-noise for phase contrast can be found in a previous thesis [120]. A few points are added here as they relate to *non-destructive* imaging in practice. For the sake of discussion, the atom cloud is assumed to induce a small phase shift $\xi \ll 1$; then the phase contrast signal is $S \sim 2\xi$. The number of spontaneously scattered photons during the imaging is $N_{sc} \propto I\xi^2$ where I is the probe intensity incident on the atoms. Thus, the destructiveness, characterized by N_{sc} , can be reduced by decreasing the intensity or increasing the probe detuning δ since $\xi \propto 1/\delta$. However, signal-to-noise represents a different issue. If the signal is assumed to be shot-noise limited then $S/N \sim \sqrt{I}\xi$. We can improve the signal-to-noise ratio by either increasing the intensity or detuning closer to boost the phase shift. Which is preferable to reduce destructiveness? The answer is that it does not matter because the signal-to-noise depends only on the spontaneous scattering rate: $S/N \propto N_{sc}^{1/2}$. Therefore, in the shot-noise limit the signal-to-noise is fixed by the scattering rate allowed for a stipulated destructiveness.

On the other hand, most of the time the image noise is dominated by background interference fringes proportional to the incident intensity. In this case, the signal-to-noise is $S/N \sim 2\xi/\eta$ where η characterizes the strength of the fringes. Under these circumstances, if the peak density of clouds being imaged is low, for example in the case of thermal clouds, the only way to obtain better signal-to-noise is to tune the probe closer to resonance. The intensity then is dropped to preserve nondestructiveness as much as possible. At some point the intensity is low enough that the shot noise becomes of the same order as the fringe noise.

The destructive nature of the probe laser has been studied by shining it continuously on the condensate. A typical result is shown in Figure 2.11(a). The decay of total

condensate number matches fairly well with the calculated spontaneous decay rate (1.5 times smaller), assuming a single frequency for the probe. The destructiveness can be considerably worse if, for example, the probe laser is running poorly single-mode.

When actually taking images, the probe does not shine continuously but is pulsed on only for brief periods of exposure ($100\mu\text{s}$). To assess any delayed heating effect following a probe pulse, a sequence of eight images has been taken using three different time intervals and a deliberately destructive probe intensity [Fig. 2.11(b)]. Only a relatively small difference in condensate loss is seen between the image sequence lasting 0.14s and the one lasting 4s, indicating that most of the atom loss due to the probe pulse occurs during the pulse time and not as a result of delayed heating.

2.5.2 Stark effects and measurement induced squeezing

Nondestructive phase-contrast imaging of condensates offers the intriguing possibility to produce measurement-induced squeezed states of atom number [57, 71], analogous to squeezed states for photons. A familiar concept from quantum optics is the existence of an uncertainty relation between photon number and phase, $\delta N \delta \xi \geq 1$. At the quantum limit where the equality sign is satisfied, a reduction of number fluctuations results in an increased variance in the phase. For a maximally squeezed state ($\delta N \sim 1$), the phase is undefined. One can argue formally that the number-phase uncertainty relation is a feature of all systems of indistinguishable bosons and so applies to a condensate as well. This would imply that a nondestructive measurement of condensate number below the atom shot noise could create a squeezed condensate. The concomitant loss of a well-defined condensate phase can be thought of as the back-action effect of the number measurement. This formal discussion has not identified the physical mechanism for the back-action. The object of this section is to show how shot noise on the probe laser intensity together with the ac Stark effect [3] produce the destructive effect on the atoms' phase. In the spirit of the "Heisenberg microscope," a direct consideration of an

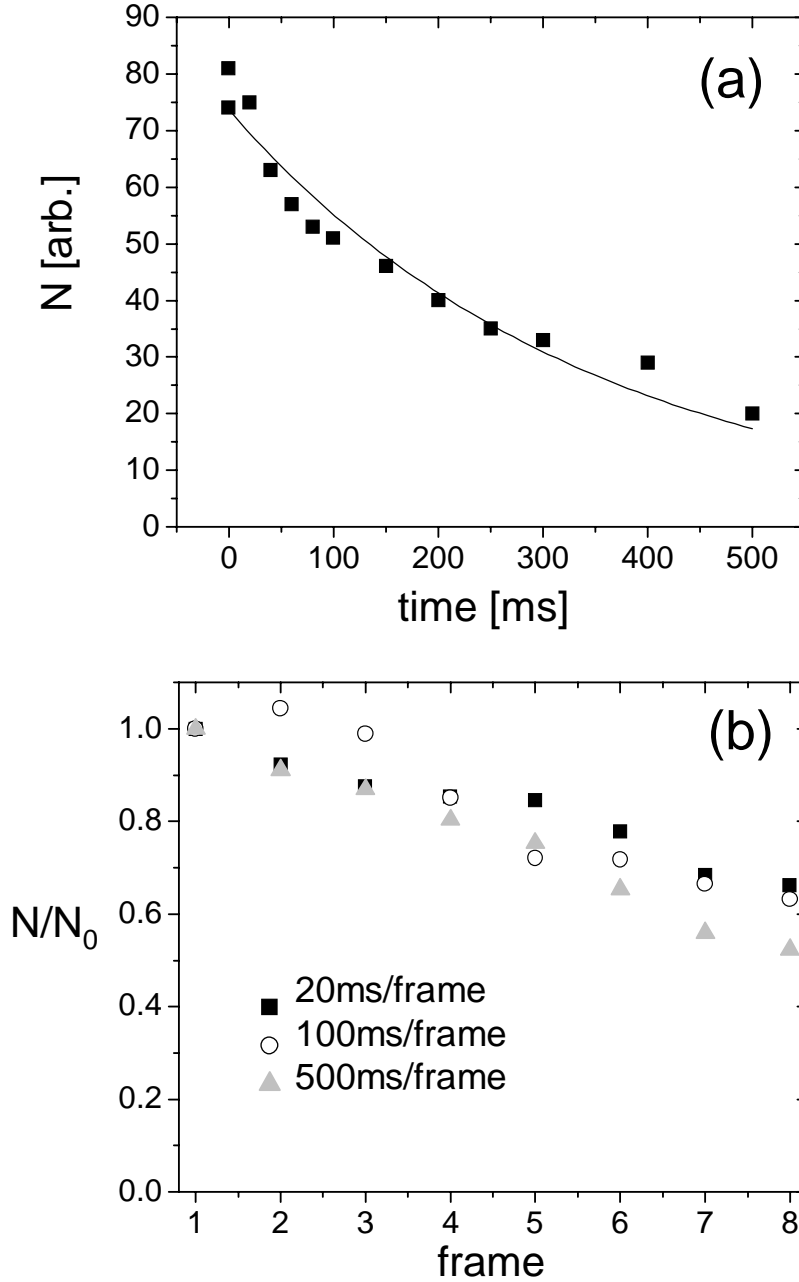


Figure 2.11: Destructive number reduction of a condensate in the presence of an off-resonant probe laser. (a) Condensate number decay due to a continuously shining probe laser with an intensity of $150\mu W/cm^2$ and a detuning of 2.1GHz from the $F = 1 \rightarrow F' = 0$ resonance. The fit exponential decay rate is $2.9(2)s^{-1}$ compared to a calculated spontaneous scattering rate of $1.9s^{-1}$. (b) Time sequence of eight probe frames with three different time intervals between frames. The light pulses for each frame are $100\mu s$ long with a large probe intensity of $2500\mu W/cm^2$ (a factor of 10 larger than typical) and a detuning of 1.1GHz from the $F = 1 \rightarrow F' = 0$ resonance.

experiment is used to arrive at the number-phase uncertainty relation for a condensate. A side benefit is a brief assessment of the feasibility to obtain number squeezing with phase-contrast imaging.

Number-squeezing due to interatomic interactions has already been observed in multi-condensate systems [132, 93]. The loss of interference contrast between the individual condensates provides a signature for the large variance in relative phase. An experiment to observe measurement-induced squeezing would use a similar technique. For example, optical tweezers can be used to split a condensate spatially into two, one of which is reserved as a phase reference. The other condensate is then subjected to a nondestructive probe, after which the condensates are re-interfered to assess the probe's affect on their relative phase. An interesting alternative that does not require any spatial separation makes use of a condensate composed of two internal spin states together with a coherent coupling drive to create a beamsplitter in the time domain. A coupled two-component condensate composed of the simultaneously magnetically trapped hyperfine states $|1, -1\rangle$ and $|2, 1\rangle$ [Fig. 2.4] has already been realized with this experimental apparatus [120] and is covered in more detail in Chapter 3. A key feature of this system is that phase contrast imaging can distinguish between the two states without needing to spatially separate them. The probe laser frequency is detuned between the two states such that the $|1, -1\rangle$ state imparts a positive phase shift to the probe beam while the $|2, 1\rangle$ state imparts a negative phase shift. As a result, in the presence of both states the net phase-contrast signal provides a direct readout of the number difference.

To simplify the discussion, the phase-contrast imaging of a single-component condensate is considered. The generalization to two components is straight forward and leads to similar results. The phase-contrast signal collected on the CCD camera provides a measure of the optical phase shift ξ imparted by the condensate, which in turn

is proportional to its column density $\bar{n}(x, y)$,

$$\xi = \beta_{pc} \bar{n}(x, y) \quad (2.37)$$

where β_{pc} is a constant which can be determined from the previous sections of this chapter. To obtain the total number of atoms in the condensate, the image needs to be integrated over all N_{pix} CCD pixels spanned by the condensate profile. The uncertainty in the total number of atoms for small phase shifts is thus

$$\delta N_{at} = \frac{1}{\beta_{pc}} \frac{A_{pix}}{m} \left(\sum_{i=1}^{N_{pix}} \delta \xi_i^2 \right)^{1/2}. \quad (2.38)$$

In the above equation, A_{pix} is the area of a pixel, m accounts for the imaging magnification, and $\delta \xi_i$ is the phase uncertainty at the i^{th} pixel. Neglecting technical noise, the output of the probe is very nearly a coherent state satisfying the uncertainty relation $\delta N_{ph} \delta \xi_{ph} \sim 1$ and having shot-noise fluctuations about the average photon number, $\delta N_{ph} \sim N_{ph}^{1/2}$. The uncertainty relation applies at each CCD pixel where N_{ph} is the number of photons arriving at that pixel. For small phase shifts, the number of photons will be approximately pixel-independent, allowing the uncertainty in atom number to be reduced to the simple result

$$\delta N_{at} = \frac{1}{\beta_{pc}} \frac{A_{pix}}{m} \left(\frac{N_{pix}}{\eta_{QE}} \right)^{1/2} \delta \xi_{ph} \quad (2.39)$$

where $\delta \xi_{ph} \approx 1/N_{ph}^{1/2}$. The coefficient η_{QE} has been added to account for the quantum efficiency of the CCD detector. To connect with experimental parameters, the number of photons at a CCD pixel can further be written in terms of the probe intensity I incident on the atoms

$$N_{ph} = \frac{\tau}{\hbar \omega} \frac{A_{pix}}{m} I \quad (2.40)$$

The various constants include the probe duration τ , the laser frequency ω , the pixel area A_{pix} and the magnification of the imaging system m .

Now that the nondestructive number measurement has been dealt with, it only remains to consider the backaction effect on the condensate phase. The off-resonant

probe induces an ac Stark shift in the internal energy state of the condensate atoms, resulting in an intensity-dependent phase shift

$$\xi_{at} = \frac{\tau\beta_{st}}{\hbar\omega} I \quad (2.41)$$

The constant β_{st} can be determined from perturbation theory for weak intensities. The *average* phase shift accumulated by the condensate can always be taken into account from a measure of the average probe intensity; what remains, however, is the uncertainty introduced by fluctuations in the intensity. Equation 2.40 can be used to relate the intensity at the atoms to the photon number counted by the CCD. This allows the uncertainty in condensate phase to be expressed in terms of the photon counting statistics at the detector,

$$\delta\xi_{at} = \beta_{st} \frac{m}{A_{pix}} \delta N_{ph} \quad (2.42)$$

The uncertainties for atom number [Eqn. 2.39] and phase [Eqn. 2.42] can be combined to yield the uncertainty relation

$$\delta N_{at} \delta \xi_{at} \sim \left\{ \frac{\beta_{st}}{\beta_{pc}} \right\} \left(\frac{N_{pix}}{\eta_{QE}} \right)^{1/2} \underbrace{(\delta N_{ph} \delta \xi_{ph})}_{\sim 1} \quad (2.43)$$

Thus the nondestructive measurement transfers the uncertainty relation for the probe photons to one for the atoms. For simple probe arrangements, for example using a single circular polarization and a magnetic bias field aligned along the imaging axis, the expression β_{st}/β_{pc} in Eqn. 2.43 is equal to one (and is expected to be larger than one for more complicated situations). In the limit of a single CCD pixel and unity quantum efficiency η_{QE} , the uncertainty relation for the atoms reaches the quantum limit expected for a system of indistinguishable bosons.

The final point addressed in this section is the feasibility of squeezing the fluctuations in condensate number with a nondestructive probe. Measurement-induced squeezing is achieved by a determination of the number to better than the atom shot-noise. The degree of squeezing can be assessed from the measurement uncertainty Eqn. 2.39

assuming an ideal detector with 100% efficiency. A practical limitation to this process is the fraction of condensate atoms lost as a result of spontaneous scattering from the probe. Clearly, the squeezing is not useful if the probe also destroys the condensate. The number of scattered photons during the probe pulse is $N_{sc} = N_{at}\Gamma\tau$ with Γ being the spontaneous scattering rate [124]. For a simple probe configuration with large detuning, the number uncertainty [Eqn. 2.39] for an ideal detector is easily written in terms of N_{sc}

$$\delta N_{at} = \left(\frac{A_c}{\sigma c_*} \right)^{1/2} \left(\frac{N_{at}}{N_{sc}} \right)^{1/2} \quad (2.44)$$

The value of the coefficient c_* is of order unity or less and, in general, depends on several Clebsch-Gordon coefficients [Eqn. 2.13] as well as the probe detuning. If a cycling transition is being used for probing, then $c_* = 1$, independent of detuning. The quantity $\sigma \sim \lambda^2/2$ is the on-resonant light scattering crosssection [Eqn. 2.8] whereas $A_c = \frac{N_{pix}A_{pix}}{m}$ is the crosssectional area of the condensate in terms of detector variables with the following qualification: The crosssectional area is $\sim \pi R_C^2$ for a condensate with radius R_C that is larger than the diffraction limit; otherwise, $A_C \sim \pi\lambda^2$ and the first term in Eqn. 2.44 attains a minimum value $(A_c/\sigma)^{1/2} \sim 1$. For typical experimental parameters, a more appropriate value for this ratio is 10 – 100. Therefore, to achieve a maximally squeezed state ($\delta N \sim 1$), the number of scattered photons needs to be at least as large as the atom number if not larger, assuredly killing the condensate [see Section 2.5.1].

Even if the squeezing is not maximal, a reasonable effect such that $\delta N_{at} = N_{at}^{1/2}/\alpha$ with $\alpha > 1$ could nevertheless be useful for atom-interferometric applications. What considerations limit the maximum value of α ? There are a number of possibilities in connection with spontaneous scattering. First, the condensate number may be so heavily depleted following the probe measurement that δN_{at} , albeit absolutely small, is not *fractionally* small anymore. This does not represent a significant limitation and

only plays a role if an overwhelming fraction of the condensate is destroyed. The second limit is reached when the uncertainty δN_{sc} in the number removed from the condensate becomes comparable to the uncertainty δN_{at} of the number measurement. This limit has some flexibility with regard to probe detuning and a discussion is left to a more detailed treatment. Instead, a third issue is briefly considered here, whereby the squeezing can be strongly limited by the maximum particle density achievable in the condensate. The maximum value of the density is determined by the rate of density-dependent inelastic loss, which depends on the atomic species being used. The resulting limitation to number squeezing can be seen to arise as follows: With $\delta N_{at} = N_{at}^{1/2}/\alpha$, Eqn. 2.44 can be solved for α :

$$\alpha = \left(N_{sc} \frac{\sigma c_*}{A_c} \right)^{1/2} \quad (2.45)$$

It is evident that the level of squeezing is connected to the number N_{sc} of photons that are spontaneously scattered. The ultimate limit to N_{sc} is on the order of the number of atoms N_{at} . This leads to a maximum value of $\alpha = \alpha_{max}$, which can be expressed explicitly in terms of the number density $n \sim N_{at}/(A_c L)$. Here, L is the size of the third dimension of the condensate. The net expression for α_{max} is given by

$$\alpha_{max} \sim \left(n \lambda^3 \frac{L c_*}{2\lambda} \right)^{1/2} \quad (2.46)$$

For ^{87}Rb , the maximum density is about $n \approx 10^{14} \text{ cm}^{-3}$, yielding $n\lambda^3 \sim 100$. The size L depends on the number of atoms and the trapping arrangement. As a specific example, in a lithographic microtrap where atom interferometry may be realized, approximate parameters include $N_{at} \sim 10^4$ and $L/\lambda \sim 1 - 10$ [4]. As a result, the limit to squeezing imposed by a finite density is roughly $\alpha_{max} \sim 10$, which is a factor of 10 less than maximal squeezing. Of course, such a value is an upper limit based on a considerable loss of atoms. The practical value of α_{max} will be lower depending on such issues as how many atoms must be preserved to achieve good detection signal-to-noise.

A significant improvement to this situation can be achieved by wrapping an optical

cavity with finesse \mathcal{F} around the atoms. This has two effects, (i) to increase the effective path length through the atom cloud (and optical phase shift) by \mathcal{F}/π and (ii) to boost the intensity in the cavity by \mathcal{F}/π relative to the input [143]. If the intensity into the cavity is reduced to maintain a given amount of spontaneous scattering, the shot-noise of the phase-contrast image will certainly increase by $\sqrt{\mathcal{F}/\pi}$; however, the image signal itself increases much more - by \mathcal{F}/π - due to the cavity-enhancement of the phase shift. The net result is a significant reduction in the number fluctuations,

$$(\delta N)_{cavity} = (\delta N)_{free} \left(\frac{\pi}{\mathcal{F}} \right)^{1/2} \quad (2.47)$$

with the cavity-free expression $(\delta N)_{free}$ given by Eqn. 2.44. At least a factor of ~ 10 improvement in the squeezing could be achieved with a reasonable finesse of $\mathcal{F} \sim 10^3$.